Astron. Astrophys. 362, 310–324 (2000)

ASTRONOMY AND ASTROPHYSICS

Mid-infrared imaging and spectrophotometry of N 66 in the SMC with ISOCAM⋆

A. Contursi[1,2,3], J. Lequeux[2], D. Cesarsky[4], F. Boulanger[4], M. Rubio[7], M. Hanus[2], M. Sauvage[1], D. Tran[6], A. Bosma[5], S. Madden[1], and L. Vigroux[1]

[1] SAp/DAPNIA/DSM, CEA-Saclay, 91191 Gif sur Yvette CEDEX, France
[2] DEMIRM, Observatoire de Paris, 61 Avenue de l'Observatoire, 75014 Paris, France
[3] IPAC, Caltech, MS 100–22, Pasadena, CA 91125, USA
[4] Institut d'Astrophysique Spatiale, Bat. 121, Université Paris XI, 91450 Orsay CEDEX, France
[5] Observatoire de Marseille, 2 Place le Verrier, 13248 Marseille CEDEX, France
[6] Max-Planck-Institut für Extraterrestrische Physik, Postfach 1603, 85740 Garching, Germany
[7] Departamento de Astronomia, Universidad de Chile, Casilla 360D, Santiago, Chile

Received 23 September 1999 / Accepted 25 May 2000

Abstract. We present observations with the mid–infrared camera ISOCAM on board the *Infrared Space Observatory* of the major star–forming region N 66 in the Small Magellanic Cloud (SMC) and of its surroundings. These observations were performed with broad filters and Circular Variable Filters giving a spectral resolution of about 40. In addition, CO(2–1) data are presented, allowing us to identify and study how hot dust relates with the different phases of the Interstellar Medium (ISM) present in N66. The spectra are dominated by the strong emission of fine-structure line. Monochromatic maps have been made in the [Ne III] 15.6 μm and [S IV] 10.5 μm line. There are significant differences between their distributions, due to the effects of density and of shocks. Aromatic Infrared Bands (AIBs) are seen at various places in the field but they are generally faint. They exhibit a variety of shapes and relative intensities, suggesting that a diversity of carbonaceous materials are present. Silicate emission is also clearly visible in the central condensation and in a few others and emission from hot small grains (Very Small Grains, VSGs) longward of 10 μm is present in the whole region. All these dust components are heated by the very strong far–UV radiation of the many young, massive stars contained in the region. The interstellar radiation field (ISRF) at 1600 Å is $\geq 10^5$ times the ISRF of the solar neighborhood in the peaks of mid–infrared emission. The relative contributions of these components (AIB carriers, VSGs and silicate grains) to the mid–infrared spectra seem to depend on the intensity and the hardness of the far–UV field. In general the 15/6.75 μm intensity ratio is higher than in relatively quiescent galactic regions (Cesarsky et al. 1996a, Abergel et al. 1996) but it is not as high as expected for a linear increase with ISRF. We interpret this behavior as due to the destruction of both AIBs carriers and VSGs in a very high ISRF. Finally several stars have been detected at 6.75 μm. Two are red supergiants; the other stars are blue and the IR emission is due to circumstellar matter or to interstellar matter heated by the star.

Key words: ISM: individual objects: N 66 (SMC) – galaxies: Magellanic Clouds – ISM: H II regions – ISM: dust, extinction – infrared: ISM: continuum – infrared: ISM: lines and bands

1. Introduction

N 66 (Henize et al. 1956) is the largest and most luminous H II region in the Small Magellanic Cloud (SMC, m-M=18.94 Laney & Stobie 1994). It is also known as DEM S103 (Davies et al. 1976) or NGC 346 referring to the main exciting star cluster.

Radio continuum observations (Taisheng Ye et al. 1991) and low–resolution Hα observations (Le Coarer et al. 1993, Fig. 1) show that the brightest emission region, N 66, is along and to the SW of an oblique (SE–NW) "bar". A more compact H II region is located at α(J2000)=00h 59m 16s, δ(J2000)=-72°10′ is N 66A. A supernova remnant is located to the East of the region.

A dense cluster of massive young stars is located in N 66, but there are also young stars outside, in particular the ionizing stars of N 66A. Massey et al. (1989) have performed an extensive study of the stellar content of the region, which contains at least 33 O stars, including 11 of type O6.5 or earlier. 22 of these O stars are contained in the central star cluster, and the others are isolated or in small groups. The hottest star, W 3 is classified O3 III(f*) (Walborn & Blades 1986). The most massive star W 1 of the central cluster, classified O4 III(n)(f) by Walborn & Blades (1986), is in fact multiple and the mass of the brightest component is at most 85 $M_\odot$ (Heydari-Malayeri & Hutsemékers 1991). The brightest star in the whole region is HD 5980, a OB?+WN eclipsing binary with V $\approx$ 11.5 (see for a recent study Heydari-Malayeri et al. 1997); it is located outside the dense

Send offprint requests to: A. Contursi (contursi@ipac.caltech.edu)

⋆ Based on observations with ISO, an ESA project with instruments funded by ESA member states (especially the PI countries: France, Germany, the Netherlands and the United Kingdom) and with the participation of ISAS and NASA.

cluster. The region was mapped in the CO(2–1) line with the SEST telescope and the results are shown here for the first time. These data show that N66 does not contain much molecular gas, except for a small cloud to the NE of the bar. The whole region has been recently reobserved in the CO(2–1) line with the SEST at higher sensitivity. These new observations show that there is also weak molecular emission in the N66 bar, connected with the H II region but not associated with the cloud detected previously both spatially and in the velocity space (Rubio et al. 2000). The region is also deficient in H I (Staveley–Smith et al. 1997) and the weak 21–cm line emission detected in this area shows no correlation with the components of N 66 and may be unrelated. Probably most of the gas is ionized outside the molecular clouds. A broad area including the region we studied has been mapped at 68″ resolution in the [C II] 157 μm line by Israël & Maloney (1993); the intensity peaks on the bar.

In this paper we present mid-IR spectrophotometric observations of N 66 obtained with the 32×32 pixel ISOCAM camera on board the *Infrared Space Observatory* (ISO) of the European Space Agency. These observations belong to a wider program aimed to study the interplay between the interstellar medium (ISM) and star formation in our and in external nearby galaxies. The Magellanic Clouds represented obvious sources to include in this project because of their proximity but also because they offer the opportunity to study how metallicity influences this process. Thus, many HII complexes in both the Large and the Small Magellanic Clouds were observed with ISOCAM in spectro-imaging mode between 5 and 18 μm and N66 is one of these sources. A 6′×6′ field centered on N66 was mapped in 7 broad–band filters and the central 3′×3′ have been observed with the Circular Variable Filters (CVFs) as dispersive elements. These observations provide a wealth of data on warm dust, fine–structure line and Aromatic Infrared Bands (AIBs).

The present paper describes the observations, their reduction (Sect. 2) and the analysis of the whole region. We will investigate the distribution of the fine–structure line emission in Sect. 3, of the dust emission of both discrete peaks and diffuse regions in Sects. 4 and 5. Sect. 6 gives the conclusions. Appendix A describes how we built the ISRF map at 1600 Å and Appendix B contains a short discussion of the stars seen in our observations.

2. Observations

2.1. ISOCAM observations and data reduction

The observations were obtained with ISOCAM in September 1996 using a 6″×6″ pixel field of view for the 32×32 element mid-infrared camera, covering a 3′ field of view for each array pointing (see Cesarsky et al. 1996 for a complete description). The observations made with the broad filters were performed as square 3×3–step raster maps with a shift (*i.e.* overlap) of 16 pixels between successive positions giving a final total field of view of 7.8′×7.8′. The integration time was 2.1 seconds (time for one exposure). A number of exposures varying from 7 to 17 according to the filter were eliminated at the beginning of each raster map. An additional 15 exposures were taken for each raster position for all the filters in order to insure better stability of the detectors, which carry remanents of their previous illumination history. The integration times were thus 283.5 seconds per filter. The filters were LW2 (5.0–8.0 μm), LW3 (12.0–18.0 μm), LW4 (5.5–6.5 μm), LW6 (7.0–8.5 μm), LW7 (8.5–10.7 μm), LW8 (10.7–12.0 μm) and LW10 (8.0–15.0 μm). The raw data were then processed in the usual way using the CIA software[1]. A library dark current was subtracted form the broad filter data and a flat–field correction was made with a flat field constructed from the data themselves. The new transient correction described by Coulais & Abergel (1999) does not give reliable results for the bright point–like sources. We thus treated the broad band ISOCAM images with the software built by Starck et al. (1999, inversion method). Corrections for field distortion have been applied to filter images before combining them in each raster. A second–order flat–field correction was finally used to match the levels on contiguous edges of the elementary maps of the rasters. This correction is only of a few percent and affects the photometry in a negligible way. The zodiacal light background used for the raster maps was the lowest emission level in each broad band image. This eliminates efficiently the zodiacal light which is distributed uniformly, but not if very extended emission is present.

Full scans of the two CVFs in the long–wavelength channel of the camera have been performed by decreasing wavelengths in April 1997. The total covered wavelength range was 5.15 to 16.5 μm. Each wavelength was observed 12 times in each scan leg, with an elementary integration time per measurement of 2.1 second. The total observing time was 4500 seconds, almost entirely used on–source. To correct the raw data for the dark current we used the dark model developed by Biviano et al. (1999) that takes into account the variation of the dark current inside a single revolution and among all the revolutions. Then, the data was deglitched and corrected for the transient response of the detector. Once again we applied two transient methods, the inversion method (Starck et al., 1999) and that which uses the Fouks–Schubert equations (Coulais & Abergel 1999). The latter method gives unreliable results in the short channel of the CVF, with negative flux for most of the pixels (before zodiacal light subtraction). This is probably due to an overestimation of the dark current which should also be corrected for the transient response. Thus to be coherent with the adopted raster map transient correction, we present here the CVF observations corrected with the inversion method. Flat fielding was done using dedicated CVF zodiacal measurements that take into account the stray–light due to the mirror and reflections between the CVFs and the detector (Boulanger, private communication).

The background of the maps is dominated by zodiacal emission that must be subtracted. The whole field of the CVF observations also collects extended emission of the N66 region, preventing us from measuring and subtracting the zodiacal light using the classical methods. In order to correct for zodiacal emis-

[1] CIA is a joint development by the ESA Astrophysics Division and the ISOCAM Consortium led by the ISOCAM PI, C. Cesarsky, Direction des Sciences de la Matière, C.E.A., France

sion, we used the redundancy between the raster maps and the CVF observations in the following way:

1. We verified that the background emission of the raster maps is consistent with the COBE–DIRBE zodiacal light measurements scaled for the single orbit in which all the maps were made (Reach, private communication). Due to the small size of the observed field and to the high ecliptic latitude we can safely assume that the zodiacal emission is uniform over the field.
2. We measured in the raster maps, using Point–Spread–Function (PSF) fitting, the fluxes of point–like sources that are also seen with the CVF, and the backgrounds around them. For all these sources, we then obtained a measure of the sum of the zodiacal background and of the diffuse SMC background in the 7 broad–band filters.
3. We built the equivalent of the broad–band filter images from the CVF data cube using the transmission curves of the filters given in the ISOCAM cookbook, and made the measurements of fluxes and backgrounds for the same point sources. The source fluxes provide a mutual calibration between CVF and filters. For each filter the background measurements are the sum of the diffuse emission (N66 and SMC) and of the zodiacal light. Between the two sets of observations (broad band filter and CVF) the only component that could change is the zodiacal light, since the solar elongation of the field changed between the filter and CVF observations. Thus, the ratio between the two background levels gives the variation of the zodiacal light between the two sets of data. We have found this ratio to be quite constant, equal to 1 ± 0.3 for each filter except for the two shortest–wavelengths filters for which the zodiacal emission is very low and our determination uncertain. We have thus obtained a spectrum of the zodiacal light which is approximately the same for the filters and the CVF observations.
4. The intensity of this spectrum is approximately half of that of the CVF zodiacal light spectrum published by Reach et al. (1996), due to the high latitude of the SMC. We have thus subtracted this spectrum multiplied by 0.5 from our CVF data. The final result is a position–wavelength data cube with zodiacal light subtracted from which one can extract spectra at given positions or monochromatic maps.

There is a slight position shift between the observations made with the Short–Wavelength CVF ($\lambda \leq 9\mu$m) and those made with the Long–Wavelength CVF ($\lambda \geq 9\mu$m) due to a slightly displacement of the SW–CVF and LW–CVF. Its effect is unimportant outside regions like the brightest emission peaks. In these cases we sometimes had to interpolate pixels or use the spectrum of the Short–Wavelength CVF of the adjacent pixel that matched the level of the Long–Wavelength CVF at 9 μm in order to produce a reasonable spectrum.

It should be emphasized that the reduction of ISOCAM data is not yet in its final stage. We estimate that the uncertainties in the intensities of the ISOCAM data presented here are $\simeq$30 %. The main source of uncertainty for both broad band and CVF data is the not complete correction of the detector transient response. For the CVF data an additional uncertainty arises from reflections between the CVF and the detector (Okumura 2000).

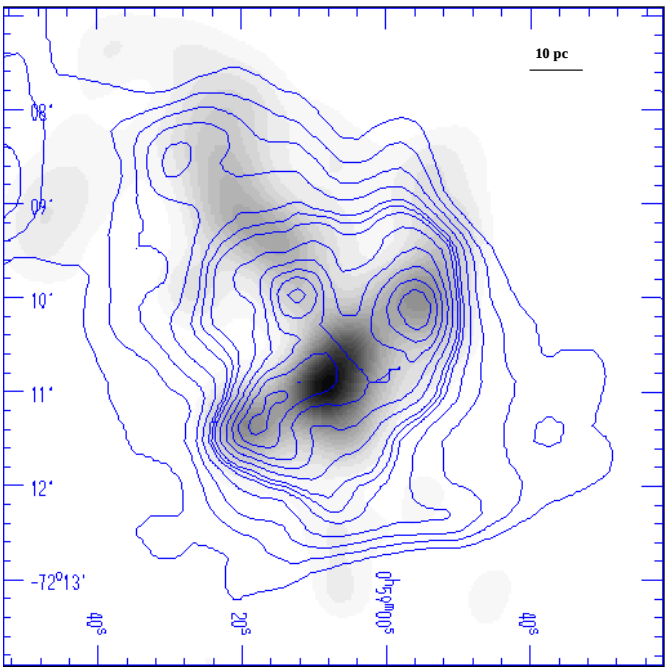

Fig. 1. Map of N 66 in the LW2 filter (6.75 μm) (grey scale) superimposed on an Hα image (contours) from the survey of Le Coarer et al. (1993) kindly communicated by Margarita Rosado. Coordinates are J2000. The LW2 image has been smoothed to the resolution of the Hα one, 9″. The SE–NW bar is more marked in the IR image than in Hα. Notice the spur in mid–IR emission extending to the NE of the bar, with no clear correspondence in Hα.

Finally, the coordinates given by the satellite were affected by errors of the order of 10″ both for filter and CVF observations. This is due to the lens jitter ($\simeq$1–2 pixels) and not to the satellite. Fortunately several stars are visible in the filter observations, and allowed the recentering of the images on the Digital Sky Survey (DSS) images (Fig. 5). The CVF frames were recentered on the filter maps using the star at 0h 59m 27s, -72° 09′ 55″ (marked as 755 on Figs. 2 and 5) which is detected in the 5 μm continuum map built from the CVF (Fig. 2). Fig. 1 shows the general outline of the filter observations as a map in the LW2 filter (6.75 μm) superimposed on an Hα image.

2.2. CO observations and data reduction

Observations of the CO(2–1) emission line at 230 GHz were obtained as part of the ESO-SEST Key program: CO in the Magellanic Clouds. The SEST telescope, located at La Silla Observatory (Chile) has a 15m diameter and a FWHM beam at 230GHz of 22″. The backend used for the observations was a 2000 channel acousto-optical spectrometer (AOS) with a total bandwidth of 86 MHz and a channel width of 0.043 MHz. At the frequency of the ^{12}CO(2–1) line the velocity range is 112 km s^{-1} and the velocity resolution is 0.056 km s^{-1}. The observations were done in the position–switch mode, with a reference posi-

tion far from the known CO emission zones. The receiver was a SIS mixer with system temperature of about 500 K. Intensity values were calibrated using the chopper wheel technique. The intensities are given in T_A^* (Kutner & Ulich 1981) and they take into account the correction for atmospheric attenuation and rearward spillover. To convert T_A^* to main–beam temperatures T_{mb} one has to divide T_A^* by η=0.60 at 230 GHz. Pointing was checked periodically on the SiO maser R Dor, and a calibration CO spectra towards the SMC source LIRS 49 (Rubio et al. 1996) was taken every day since R Dor could only be observed after the SMC.

Initially, N 66 was observed in the CO(1-0) emission line in a coarse grid with a $40'' \times 40''$ spacing centered at α(J2000)= 0h 59m 07.5s, δ(J2000)= -72° 10′ 26″. This grid includes the entire field studied with ISO. Emission was found at the offset position (80″, -80″) and a fully–sampled map was done in the CO(1–0) line around this region (see Rubio et al. 1996). To improve the spatial resolution and derive the physical properties of the molecular cloud, N 66 was later fully mapped at 10″ spacings, about half the HPBW of the SEST, in the CO(2–1) emission line. A 10 × 11 grid was made, each position observed with an integration time of 240 seconds giving an r.m.s. noise of 0.1K per channel. The 230 GHz observations were made with half of the high resolution backend, the other half being connected to the 115 GHz receiver. The spectra were smoothed and a linear baseline was removed.

A contour map of the CO(2–1) emission integrated over the velocity interval from 154 to 166 km s^{-1} is shown on Fig. 12, superimposed on the LW2 (5.0–8.0 μm) image. More recently, we discovered faint CO emission associated with the peaks shown on Fig. 5. This will be discussed in a further paper (Rubio et al. 2000.

3. The fine–structure line

The two fine–structure line [Ne III] 15.6 μm and [S IV] 10.5 μm are prominent in the CVF spectra (see Fig. 6). The [Ne II] line at 12.8 μm is blended with the infared band (IR) at 12.7 μm, and this blend is quite faint everywhere with respect to the [Ne III] line. However, the distribution of the 12.7 IB + [NeII] emission line (not shown here) and that of the [Ne III] are very different, the former being very similar to the distribution of the 11.3 and 6.2 μm IBs. This suggests that the emission feature at 12.7–12.8 μm is dominated by the IB and that the [NeII] fine structure line is everywhere negligible. A strict lower limit for the [Ne III]/[Ne II] intensity ratio is 1.0. We can compare this lower limit to the [Ne III] 15.5μm/[Ne II] 12.8 μm intensity ratios found in other sources with ISO-SWS. Contrary to the ISOCAM instrument, SWS can separate the [Ne II] 12.8 μm emission line from the 12.7μm IB. The values found are all less than in N66, ranging from ∼0.8 in the overlapping region of the Antennae galaxy to ∼0.2 in the Galactic Center (Moorwood et al. 1996, Lutz et al. 1996, Kunze et al. 1996). On the other hand, higher [Ne III]/[Ne II] values have been observed with ISOCAM in a sample of dwarf galaxies from Madden (2000). The exceptionally large strength of the [S IV] line and the very high [Ne III]/[Ne II] ratio confirm that N 66 is a region of particularly high excitation, due to the large number of extremely hot O stars that it contains (Massey et al. 1989). This was previously known from the high electron temperatures (12000–14000 K) and the high ratio [O III]λ5007/H$\beta \approx 5$ measured at different points of the nebula (Peimbert & Torres–Peimbert 1976, Dufour & Harlow 1977, Pagel et al. 1978, Dufour et al. 1982). Fig. 3 is a map in the [S IV] 10.5 μm line superimposed on the [Ne III] 15.6 μm map.

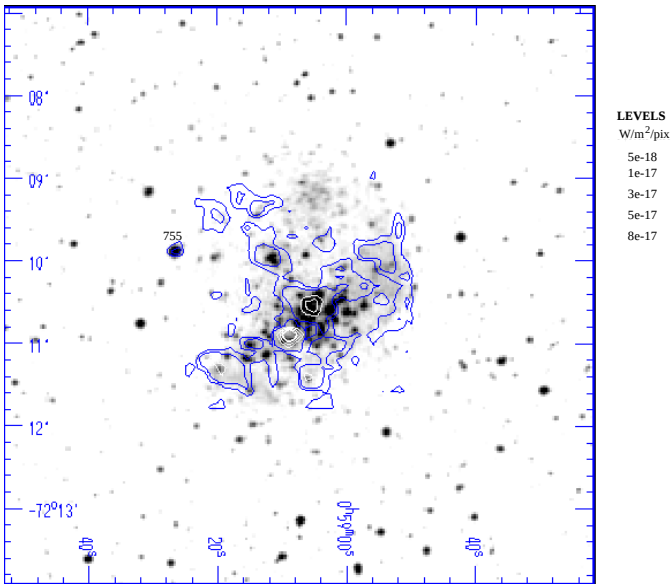

Fig. 2. CVF map of N 66 in the 5 μm continuum (contours) superimposed on the DSS image (grey). Coordinates are J2000. Star N 346-755 in the catalog of Massey et al. (1989) is marked. It has been used to recenter the CVF images on the DSS image.

By comparison with the Hα map of Fig. 1 and the radio continuum map of Taisheng Ye et al. (1991), it appears that the fine structure line emission is associated with N 66, extending over our field of view. We estimate from the radio data of Taisheng Ye et al. (1991) that the amount of energy in the Hβ line is $\approx 5\,10^{-13}$ W m^{-2} in this field. This of course is intrinsically corrected for interstellar extinction. Extinction is low (E(B-V)=0.14 according to Massey et al. (1989)), and we neglect it when considering the mid-IR observations.

An interesting feature of the [Ne III] map is the presence of several holes in the distribution of the ionized gas (Fig. 3). These holes are presumably due to previous supernova explosions or to the effects of stellar winds. The latter explanation is probably true for the central and more pronounced hole, which is near the hottest star in the N 66 OB association (an OIII(f*) star marked on Fig. 3). The differences in the distribution of the [Ne III] and [S IV] line are noteworthy. The emission in the [Ne III] line follows roughly that of Hα as far as one can judge given the different angular resolutions (compare Figs. 1 and 3). This is not the case for the [S IV] line. Most of the differences in the main emitting region are probably density effects: model calculations e.g. by Stasińska (1984) show that the [Ne III]/[S IV] line intensity ratio is decreased in regions of lower densities, the other

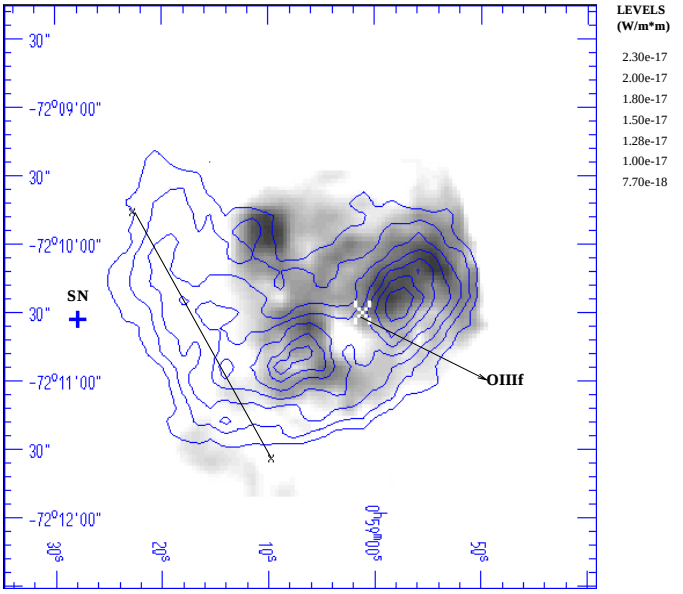

Fig. 3. CVF map of N 66 in the [S IV] 10.5 μm line (contours) superimposed on the [Ne III] 15.6 μm line map. Coordinates are J2000. Notice the holes in the [Ne III] 15.6 μm map. There are large differences between the distributions of the two line. The position of star W 3, classified O3 III(f*), is indicated by a white cross. The strong [S IV] emission to the East is presumably due to the supernova remnant SNR 0057-7226, whose center is indicated by a black cross. The solid line represents the cut along which we evaluated the line intensity profiles of Fig. 4.

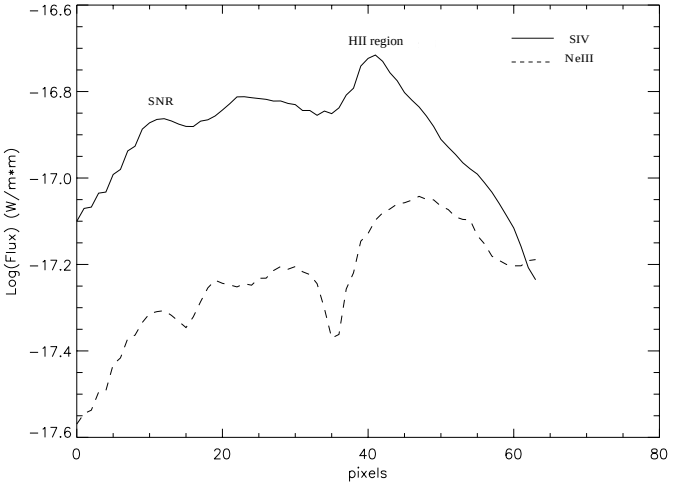

Fig. 4. The logarithmic profile in the [Ne III] 15.6 μm line (dashed line) and the [S IV] 10.5 μm line (solid line) along the cut shown in Fig. 3. Coordinates are J2000. Note that the [S IV] line intensity is always higher than that of [Ne III], the [S IV]/[Ne III] line intensity ratio reaching a maximum at a position closest to SNR.

parameters being the same. This might explain why the holes are more visible in the [Ne III] than in the [S IV] line. There is relatively less [Ne III] emission in the eastern part of the field where the emission of [S IV] is substantial; here the [S IV] line intensity is roughly twice that of [Ne III]. This region contains a faint Hα filament (not visible on Fig. 1) which is a part of the

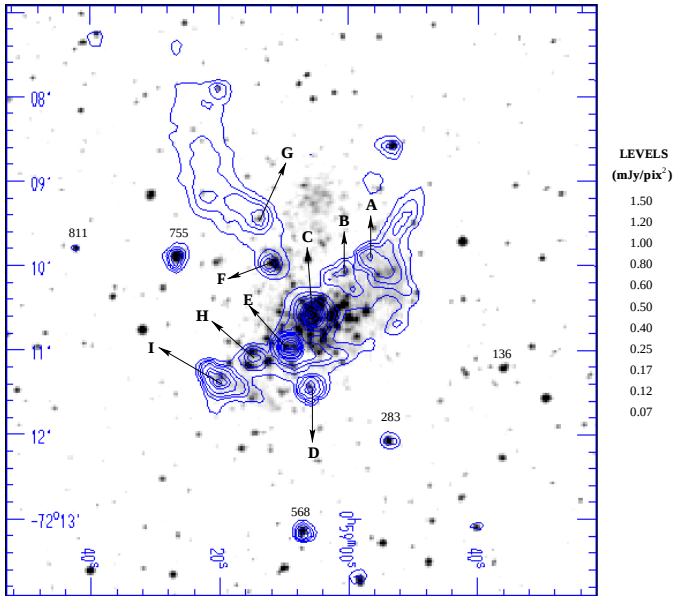

Fig. 5. Map of N 66 in the LW2 filter centered at 6.75 μm (contours), superimposed on the ESO Digital Sky Survey (DSS) image. Coordinates are J2000. Several stars are detected in the LW2 filter: they are HD 5980 (N 346-755) and 2 red stars (N 346-283 and 811: numbers in the catalogue of Massey et al. (1989), see Table 1). The red star N 66-136 is not detected. Some other stars are surrounded by an extended emission: they are blue and probably heat the surrounding interstellar matter.

supernova remnant SNR 0057-7226 (Taisheng Ye et al. 1991). The position of the center of this remnant is indicated on Fig. 3. The difference in the distributions of the [Ne III] and of the [S IV] line is best illustrated by Fig. 4 which shows the fine structure line–intensity profiles along the direction marked on Fig. 3. It appears that the emission of [S IV] is enhanced compared to that of [Ne III] by preferential shock ionization of S with respect to Ne: in high-excitation conditions Ne III is the dominant Ne ion and its abundance can only be decreased by collisional ionization, while S III and S IV have roughly the same abundances and S III will be ionized in the shock.

By integrating over the whole map, we obtain total fluxes of $\approx$ 7.3 10^{-14} W m^{-2} and $\approx$ 8.8 10^{-14} W m^{-2} in the [Ne III] and [S IV] line respectively. The [Ne III]/Hβ and the [S IV]/[Ne III] ratios are $\approx$ 0.1 and $\approx$1.2 respectively and together with the optical line ratios obtained by various authors cited above, they can be compared with the results of photoionization models. We used the models of Stasińska (1982, 1984, 1990), of Stasińska & Leitherer (1996) and of Schaerer & de Koter (1997). A fair agreement can be reached for the relative intensities of the [Ne II], the [Ne III] and the [S IV] line as well as of the [O III]$\lambda\lambda$5007, 4959 Å and 4363 Å and other visible line, using models with T_{eff} of exciting stars 40 000 to 45 000K, abundances 1/10 solar, density 10 to 100 electrons cm^{-3}. These parameters are reasonable from what we know otherwise of the H II region with its very hot exciting stars. Direct abundance effects cannot be invoked to explain the particularly high [S IV]/[Ne III] ratios, the abundance ratios [Ne/O]

(Pagel et al. 1978) and [S/O] (Dennefeld & Stasińska 1983) being approximately the same in the H II regions of the SMC and of the Galaxy. However, most of these models yield ratios of the mid–IR line of [Ne III] and [S IV] to Hβ too high by a factor 2 with respect to the observed ratios, with the exception of the old models of Stasińska (1982), which are based on the model atmospheres of Mihalas. But one should note that the optical measurements refer to the central H II region while the [Ne III] and [S IV] line intensity ratios to Hβ are global. Clearly more detailed optical studies are required in order to reach more definitive conclusions. Given the lack of data for the supernova remnant, it is premature to try to model the intensities of the [Ne III] and [S IV] line in its direction.

4. The mid-IR emission of the discrete peaks

The CVF and filter observations show strong emission peaks which we discuss here. They are ordered by increasing right ascension and named as shown in Fig. 5. This figure shows the LW2 (6.75 μm) contours superimposed to the Digital Sky Survey image of N66. The isolated stars are identified by numbers given in Massey et al. (1989). In Fig. 6 we present the CVF spectra of these peaks. Most of the spectra represent an average of two pixels: spectra of peaks C and E have been obtained averaging four pixels (1 pixel$\approx$1.2 pc for the assumed SMC distance). In general the spectra show emission bands and fine structure line on top of a continuum. The wavelengths of the emission bands correspond to those of the Unidentified Infrared Bands already observed before ISO at 6.2, 7.7, 8.6, 11.3 and 12.7 μm (Gillett, Forrest and Merrill 1973, Russell, Soifer and Merrill 1977a, Russell, Soifer and Willner 1977b, Cohen, Tielens and Allamandola 1985, Cohen and Kevin 1989, Jourdain de Muizon et al. 1986, Phillips, Airken and Roche 1984, Roche, Aitken and Smith 1989). They are an universal signature of the ISM in our (Roelfsema et al. 1996, Verstraete et al., 1996, Cesarky et al. 1996a, 1996b, Boulanger et al. 1996, Mattila et al. 1996, Uchida, Sellgren and Werner 1998) and in external galaxies (Boulade et al. 1996, Vigroux et al. 1996, Acosata–Pulido et al. 1996, Metcalfe et al. 1996, Helou et al. 2000). The exact chemical species from which these bands originate have not been yet identified. The best candidates are the Polycyclic Aromatic Hydrocarbons (PAH) (Puget and Lèger 1989), i.e. planar macro–molecules (few hundred atoms) transiently heated by single photon absorption. However, whatever is the exact nature of these carriers, the bands are certainly due to aromatic compounds. For this reason hereafter we will call them Aromatic Infrared Bands (AIBs) carriers. Fig. 6 show the following characteristics:

– Peaks A, B, C, E, H and I are aligned along the "bar"(Fig. 5). Peak C coincides with the center of the dense star cluster NGC 346. The other peaks are at various distances from this cluster and receive less far-UV radiation except perhaps Peak E. The Hα and fine–structure emission line in the direction of Peak C are relatively small, presumably because the gas has been partly expelled by stellar winds from the dense central cluster.
– Peaks D, F and G lie outside the "bar". F coincides with the compact H II region N 66A.

The CVF spectra of all these emission peaks show [Ne III] 15.6 μm and [S IV] 10.5 μm line emission (Fig. 6).

Even if emission bands are observed at the typical wavelengths of the most intense AIBs (6.2, 7.7, 8.6, 11.3 and 12.8 μm), these are very different in their shape and relative intensities from the AIBs observed in the galactic reflection nebulae, to which hereafter we will refer as the "classical" AIBs.

Peak A shows a broad AIB at 7.7 μm, a 11.3 μm AIB not very intense and faint 12.7 (possibly blended with a [Ne II] line at 12.8 μm), 13.5 and 14.5 μm bands.

Peak B shows very faint AIBs, if any, and a broad silicate emission at $\simeq$ 10 μm. Note that there are a few faint hot stars in Peak A (N 346-320 and 325), as well as in Peak B (N 346-347, 352, 353 and 357: Massey et al. 1989).

Peak C, in the direction of the center of the young star cluster, has a spectrum very similar to that of Peak B but with a stronger continuum. It exhibits only faint AIBs and a broad 10 μm silicate band is clearly seen in emission. The spectrum of Peak C is discussed in more detail by Contursi et al. (2000).

The spectrum of peak D is characterized by broad emission near 8 μm where the usual AIBs are partly merged. Note the short–wavelength continuum, also seen towards Peaks C and E. This region contains at least 3 hot stars (N 346-466, 469 and 478) the brightest of which is the evolved or reddened N 346-466 (V=15.91, U-B=-0.54:, B-V=0.27, Massey et al. 1989)

Peak E contains the relatively bright, reddened O8V star N 346-549 with V=15.26, U-B=-0.96, B-V=0.22 (Massey et al. 1989). The continuum near 5 μm is the strongest in the whole map (see Fig. 2). It is too strong to be the photospheric emission of the star, but it can be due at least in part to circumstellar dust or to a red companion. The most conspicuous feature in the spectrum of Peak E is a very broad emission feature centered near 7.7 μm in which the usual AIBs are even less identifiable than in the spectrum of peak D. Both the continuum at 5 μm and the presence of the broad band at 7.7 μm are characteristics of AGN spectra like that of Centaurus A (Mirabel et al. 1999). The origin of the 7.7 μm broad feature has not yet been established: it may be due to coal–like grains. However, it is not clear whether these types of grains normally exist in the ISM of galaxies and become visible only when destruction of classic AIBs carriers occurs, or if they form through hard UV photons processing on the classical AIB carriers. The 6.2 and 11.3 μm bands are surprisingly weak. The peculiar appearance of the 7.7 μm brad feature and the faintness of the 11.3 μm band might be due to some amount of silicate absorption, but the [S IV] line at 10.5 μm, which should also be affected, does not seem particularly weak. Moreover, the presence of a certain amount of silicate absorption cannot explain the weakness of the 6.2 μm AIB. Note also the features at 13.5 and 14.5 μm which can arise from the out–of–plane C–H bending vibrations on aromatic rings with 3 and 4 contiguous H atoms (*trio* and *quarto*).

The spectrum of Peak F (N 66A) shows probable silicate emission and weak AIBs. Peak F contains at least 7 hot stars, the

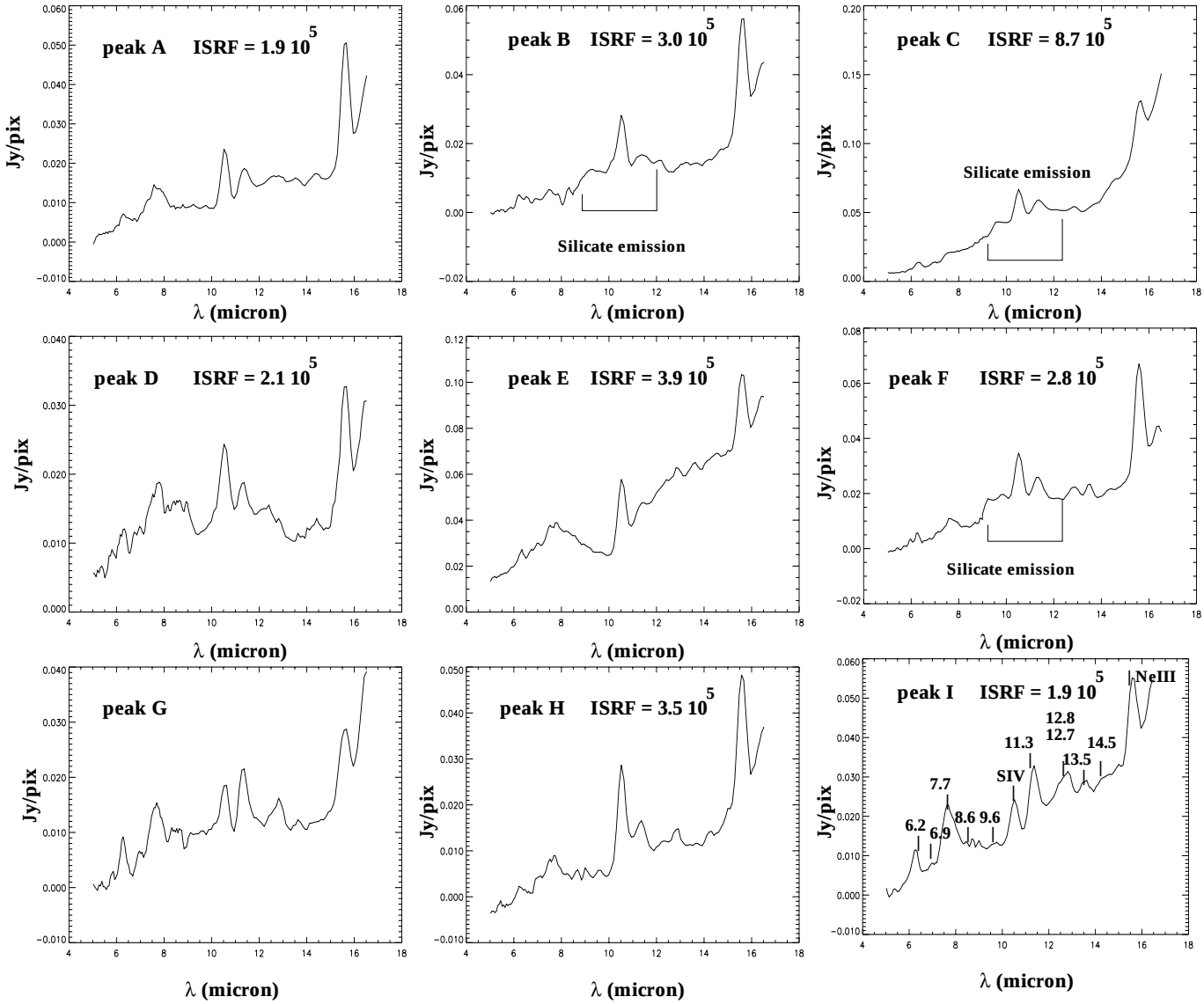

Fig. 6. CVF spectra of the 9 main emission peaks in the region of N 66. The peaks are identified on Fig. 5. These spectra have been corrected for zodiacal light as explained in Sect. 2. An estimate for the mean ISRF at 1600 Å normalized to the local ISRF at the same wavelength for each source is given. If dust is mixed with the ionized gas, these values should be decreased by a factor 2.5 (see text for details). The main fine–structure line, the visible H_2 line and AIBs (A) are identified in the spectrum of Peak I. All spectra show the [Ne III] 15.6 μm and [S IV] 10.5 μm line. The AIBs exhibit a variety of shapes and relative intensities. The broad 10 μm silicate band is seen in emission in the spectrum of Peak C and B and less obviously of Peak F.

brightest of which is the O5.5V star N 346-593 with V=14.96, U-B=-1.01, B-V=-0.16 (Massey et al. 1989).

Peak G coincides with two hot stars, N 346-628 and 635 (Massey et al. 1989). This peak is on the molecular cloud not associated with the main HII region (Fig. 12). Its spectrum is the closest to the typical Galactic AIB spectra, e.g. those of NGC 7023 (Cesarsky et al. 1996a).

Peak H has faint bands and peak I displays intense AIB bands. Both show a classical AIB spectrum. They contain a few faint hot stars, respectively N 346-640, 641, 648, 654 and N 346-696 and 697 and in fact it has a steep continuum rising toward long wavelength. Moreover, Peak I contains the bright late O or early B star N 346-690 with V=15.70, U-B=-0.75, B-V=0.00 (Massey et al. 1989) and it has the brightest emission in both CO(1–0) and H_2 among the MIR peaks (Rubio et al. 2000). The column density in this peak, relative to the others region, is thus sufficiently high to explain the strength of AIBs.

As the AIBs are believed to be excited mainly by far–UV photons in the hard radiation field of N 66, we have built a rough map of the radiation density at 160 nm using the stellar photometry from Massey et al. (1989) (Fig. 7). Details about

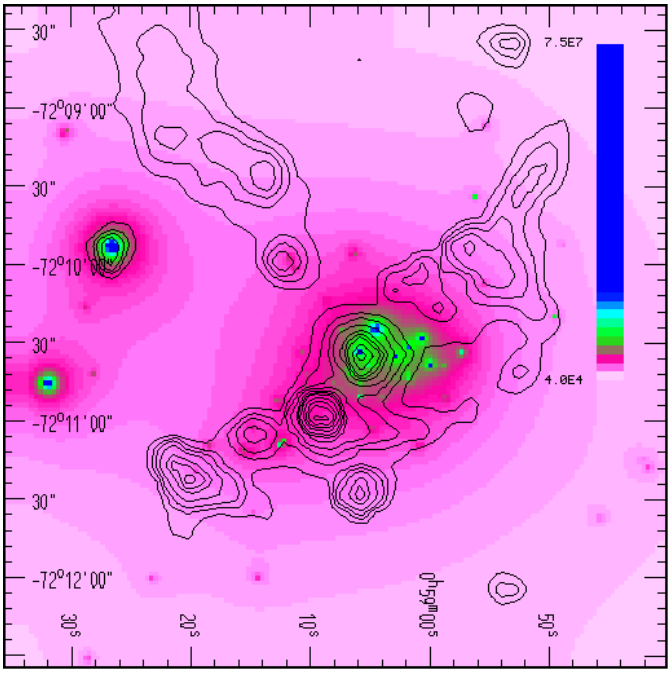

Fig. 7. Projected distribution of the radiation field at 160 nm in the region of N 66 (grey scale), superposed on the LW2 (6.75 μm) contours. Coordinates are J2000. Gray scale values are in Local ISRF units.

how we built this map are given in Appendix A. There are two sources of uncertainties in this calculation. 1) Extinction has not been taken into account (except for determining the intrinsic stellar UV flux). Extinction in N 66 is known to be very small for stars (E(B-V)=0.14, Massey et al. 1989) and the Balmer decrement value of 3.05 $\pm$ 0.15 (Ye et al. 1991) is close to the unreddened value of 2.86. If dust is mixed with the ionized gas, our values for the UV fluxes are upper limits and may be too high by $\sim$ 1 mag. (a factor 2.5). If dust is outside the ionized gas regions our values are unaffected. 2) The other uncertainty is due to errors in the assignment of the stellar spectral types. However, changing the luminosity class in the most ambiguous cases changes the radiation density by only 30%.

The average values of the ISRF at 1600 Å normalized to the local ISRF (LISRF) at the same wavelength (Gondhalekar et al. 1980) are indicated in Fig. 6 and they range from 2 to 9 $\times$ 10^5 the LISRF. They correspond to the values obtained per DSS pixel (=1.7″) averaged over a circular area of 2.8 pc radius (= 5.6 DSS pix with an assumed distance for SMC=61 kpc). This is the approximate resolution of the ISO data, thus the same aperture was used to obtained the LW3, LW2 and the 160 nm fluxes reported later in Fig. 14. Note that if dust is mixed with gas inside the HII region, the UV flux values still remain very high, ranging from 5.3 10^4 (peaks A and I) to 2.5 10^5 (peak C) times that of the solar neighborhood. In Fig. 6 we have not labeled the ISRF average value of peak G because the new CO(2–1) data show that this cloud and probably the "spur" visible as diffuse emission (see Sect. 5) are not associated with the N 66 bar (Rubio et al. 2000).

From the collection of CVF spectra that we have just discussed, several conclusions can be derived:

- Silicate emission is clearly visible in Peak C and B and more marginally in Peak F. Interstellar silicate emission has been detected in the Orion nebula and a few other H II regions, and must be due to relatively big grains (size $>$ 0.01 μm) heated to $\sim$ 100 K or more, since it is only seen when the radiation field is very high (Cesarsky et al. 2000).
- In three peaks (C, D and E), there is clear continuum emission at all the studied wavelengths down to the shortest one, 5 μm. While a part of this continuum may be associated with the AIBs, it is clear that they cannot account for all: classic Galactic AIB spectra as those of NGC 7023 or M 17 (Cesarsky et al. 1996a, 1996b) show a negligible contribution of the AIBs at 5 μm. The 5 μm continuum should then be due mostly to grains rather close to the hot stars contained in each of these regions. In Peak C relatively small silicate or other grains can be heated to sufficient temperatures to emit at 5 μm (see Contursi et al. 2000). The radiation field is lower in peaks E and D. But both peaks contain reddened stars, and the emission might be due to dust around these stars.
- The AIBs emission shows differences in the studied peaks. The AIB spectra are sometimes very different from the "typical" Galactic AIB spectra of e.g. NGC 7023 (Cesarsky et al. 1996a). The 7.7 μm band towards Peak E is much broader and the 8.6 μm band is not visible, perhaps merged into the 7.7 μm feature (but this might be partly due to silicate absorption). Peak D displays an intermediate case. "New" features near 13.5 and 14.5 μm are visible in several spectra. Although faint, these features are likely to be real. Residual from glitches could result in artificial features only for few pixels. Moreover, the same bands are also visible in other regions like M 17 and NGC 7023 (Cesarky et al. 1996a, 1996b, Klein et al. 1999). Fig. 6 shows that there is a spectral evolution from peak C, in the center of the star cluster, to peaks F, I, D and G, where the AIBs are stronger with respect to the continuum and more similar to the "classical" Galactic AIBs. This suggests that UV radiation has a crucial role on the grain processing. It destroys the classical AIB carriers, favoring the broader–band emission of relatively big carbonaceous grains which are heated to sufficient temperatures (peak E) or of smaller carbonaceous grains heated transiently by absorption of single photons. There might be transformations from PAH–like 2–D molecules responsible for the classical AIBs into 3–D grains or vice–versa. The broad band emission of peak E might indicate phenomena occurring close to the reddened O stars contained in these regions.
- The strongest AIB/continuum ratio and the most "classical" AIB spectrum is observed towards Peak G to the North of the CVF map. This peak is at the southern edge of a spur well visible in the LW2 filter images (5.0–8.0 μm) of Fig. 5. Since this spur and the molecular cloud (Fig. 9) are not associated with the N 66 star cluster (Rubio et al. 2000), grains

here are heated by an ISRF lower than in the bar, providing a spectrum more similar to those observed in relatively quiescent regions of our Galaxy.

5. The diffuse emission

The diffuse emission is better studied from the filter maps because of their higher sensitivity. However the CVF observations are useful in the interpretation of the filter observations.

There is no reason to doubt that far from the emission peaks which coincide with concentrations of hot stars, most of the radiation at wavelengths shorter than about 9 μm is due to AIBs and their associated continuum. This is already clear for Peak G (see Fig. 5) which is far from the main far–UV sources even if it contains two 16th–magnitude hot stars. Consequently, we believe that the best view of the distribution of the AIBs is offered by the LW2 (5.0–8.0 μm) map which encompasses the 6.2 and 7.7 μm features (Figs. 5 and 6), although there is some contribution from Very Small Grains (VSGs: Désert et al. 1990; Dwek et al. 1997) in the peaks where the radiation field is very high (see Fig. 6 and Cesarsky et al. 1996b). The stellar contribution in this filter is limited to that of a few red stars identified on Fig. 5, and perhaps to the emission of circumstellar dust around hot stars as discussed in the previous section. The LW6 (7.0–8.5 μm) and LW7 (8.5–10.7 μm) maps (Figs. 8 and 9) and the LW4 (5.5–6.5 μm) map (not shown) are very similar to each other and to the LW2 map, although the NE extension and some stars are more easily visible on the LW2 map which is more sensitive due to the broader passband of this filter.

The filter maps which include AIBs at longer wavelengths, e.g. the LW8 (10.7–12.0 μm, not shown) and LW10 (IRAS filter: 8.0–15.0 μm, Fig. 16) maps, are more difficult to interpret because they contain a contribution of both AIBs and VSGs.

A particularly interesting feature in the LW2 (5.0–8.0 μm) and LW6 (7.0–8.5 μm) maps is the emission spur that extends to the NE of N 66A. This spur is probably dominated by AIB emission. It is barely visible in filters like LW3 (12.0–18.0 μm) in which the contribution of AIBs is minor (see Fig. 10). Fig. 12 shows a superposition of the CO(2–1) line emission in the region of N 66 over the LW2 map. The CO emission coincides very well with the spur of AIB emission. As discussed above, this can be easily explained by emission from the surface of the molecular cloud bathed by a lower and softer radiation field than in the bar of N 66.

Fig. 10 is the LW3 (12.0–18.0 μm) map of the N 66 region. Although there is some contribution from the [Ne III] 15.6 μm line and of the [Ne II] line and AIB at 12.7 μm in the LW3 filter, our CVF spectra show that it can generally be neglected with respect to the continuum. This is shown by Fig. 11 on which the CVF image in the continuum on each side of the [Ne III] 15.6 μm line (contours) is superimposed on the LW3 image (grey scale): the agreement is very good given the differences in field of view and sensitivity. Thus the LW3 map in our case represents adequately the emission of the Very Small Grains (VSGs). It is noteworthy that the distribution in the LW3 map is more extended around the "bar" than the LW2 map although the latter is more sensitive (compare Fig. 10 with Fig. 5). This has rarely been seen before and may indicate VSG emission in regions where the AIB carriers have been partly destroyed.

Fig. 13 presents the "color" map of the LW3(12.0–18.0 μm)/LW2 (5.0–8.0 μm) intensity ratio. For building this map, the LW3 data have been convolved with the LW2 PSF as measured on the LW2 map, and vice-versa before division; this resulted in a small loss of resolving power but produced approximately similar PSFs after convolution. Then only the part

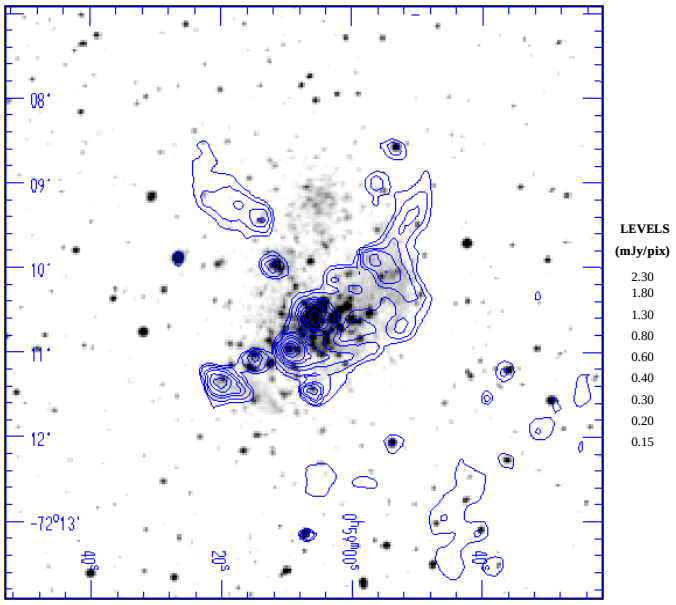

Fig. 8. Map of N 66 in the LW6 (7.0–8.5 μm) filter (contours) superimposed on the ESO Digital Sky Survey (DSS) image. Coordinates are J2000. Compare to the LW2 map (Figs. 1, 5 and 7).

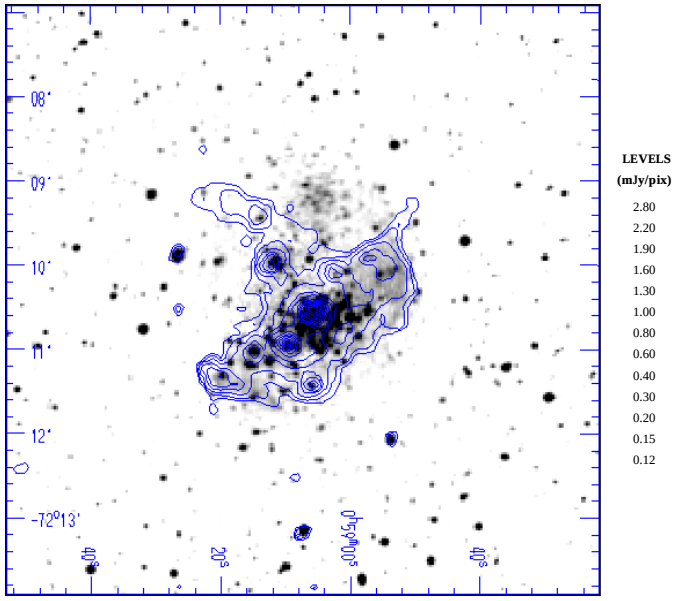

Fig. 9. Map of N 66 in the LW7 (8.5–10.7 μm) filter (contours) superimposed on the DSS image. Coordinates are J2000.

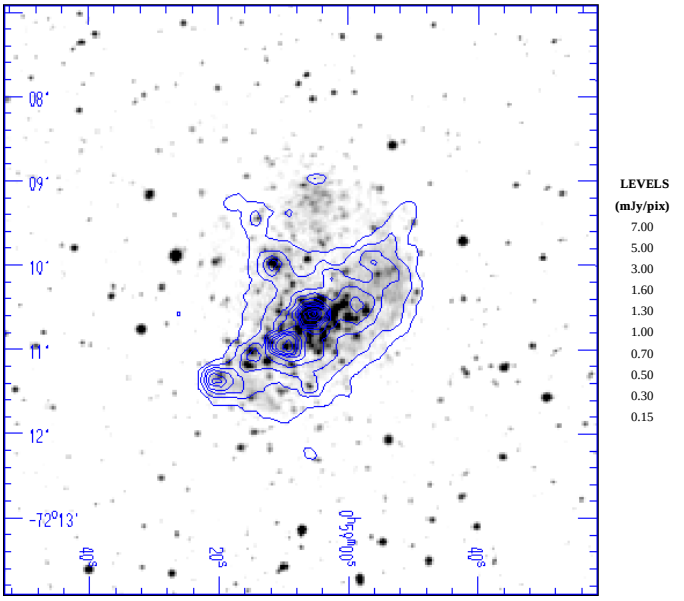

Fig. 10. Map of N 66 in the LW3 (12.0–18.0 μm) filter (contours) superimposed on the ESO Digital Sky Survey (DSS) image. Coordinates are J2000. This image show the distribution of the warm Very Small Grains (VSGs). The faint "sources" 1.5′ North and South of the main body of emission are ghosts of the main peak (Peak C) due to imperfect correction of the transient response of the detector.

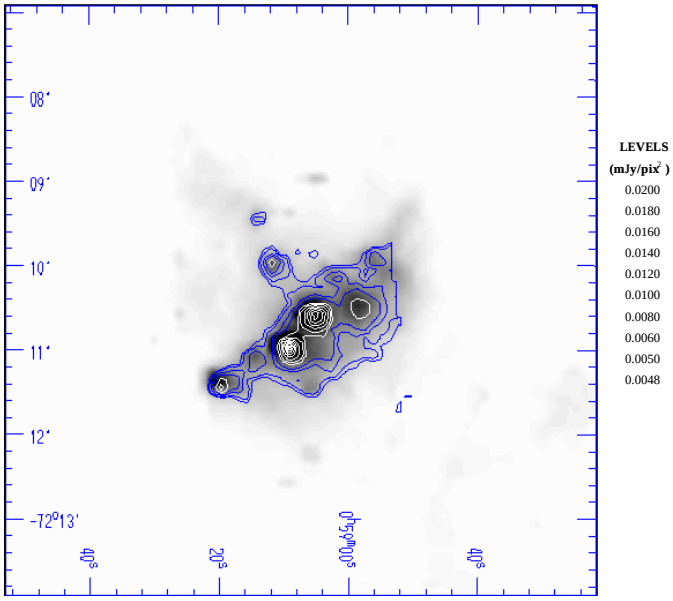

Fig. 11. Map of N 66 in the LW3 (12.0–18.0 μm) filter (grey scale) with the CVF contours of the continuum near 15.6 μm superimposed. Coordinates are J2000. The agreement is excellent except for a small position shift between the filters and the CVF. It shows that the LW3 image is dominated by continuum emission except in the NE extension, for which the contribution of the 12.7 μm AIB is strong, and to the west of the main Peak C, where the contribution of the [Ne III] emission is important.

of the data with a signal to noise ratio larger than 2 after convolution has been retained in both filters.

Previous observations with ISO (e.g. Cesarsky et al. 1996b, Contursi et al. 1998) have shown that the VSGs start to emit appreciably near 15 μm when the ultraviolet radiation field is $\geq$ a few 10^3 times the LISRF. Under these conditions the VSGs temperatures are high enough for their spectrum to shift towards short wavelengths increasing the 15/6.75 μm ratio, This ratio ranges from 0.5 to 0.8 in the LISRF environnement. The FUV values obtained in N66 indicate that the ISRF intensity is well above 10^3 times the LISRF everywhere in the observed region except in the region of the molecular cloud. In order to study how the 15/6.75 μm color ratios relate to the UV ISRF we have evaluated the 15/6.75 μm ratio of each peak over regions of the same size (radius = 2.8 pc), and plotted them as a function of the ISRF at 1600 Å integrated over the same regions (Fig. 14). As expected, the general trend is that the higher the ISRF, the higher is the 15/6.75 μm ratio. One can see that the spur (peak G) has a typical 15/6.75 μm "cirrus" value of $\simeq 1$. The same effect is observed for the global IR emission properties of galaxies. The 15/6.75 μm – 60/100 μm color–color diagram shows that the global mid-IR (15/6.75 μm) colors are $\simeq 1$ for normal galaxies ("cirrus" value) and become significantly greater than 1 for more active galaxies (Vigroux et al. 1998, Dale et al. 2000). The same behavior is also observed inside three nearby galaxies, IC 10, NGC 1313 and NGC 6946 (Dale et al. 1999).

Surprisingly, the highest value of the the 15/6.75 μm ratio in Fig. 14 does not correspond to the highest value of the ISRF, located at the center of the star cluster (peak C). The CVF spectrum of the region with the largest value of the 15/6.75 μm ratio

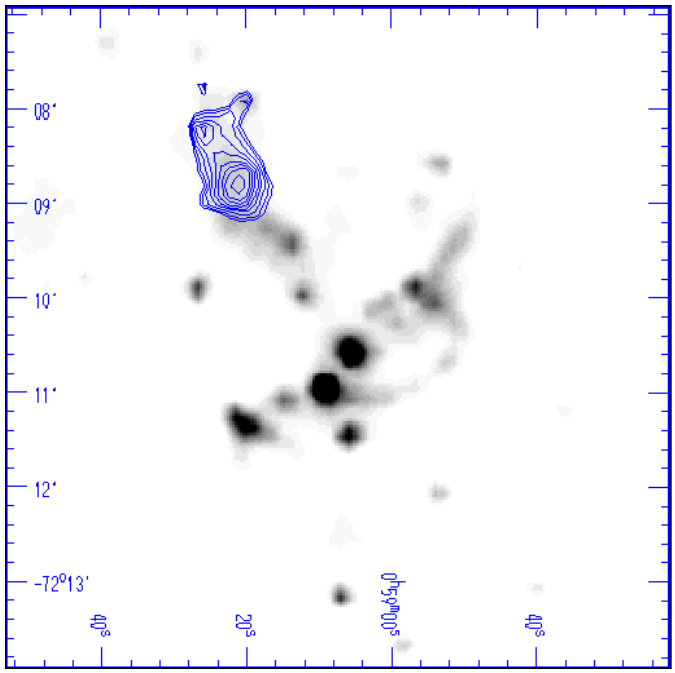

Fig. 12. CO(2–1) emission of the region of N 66 obtained with a resolution of 22″ (contours) superimposed on the LW2 (5.0–8.0 μm) image, which is dominated by the AIB emission (grey scale). Contour levels are from -0.5 ($\sim 3\sigma$) to 7.5 in steps of 0.5 K km s^{-1}, the temperature being T_A^*. Coordinates are J2000. The CO emission coincides with the NE spur of the LW2 map.

is shown on Fig. 15. Following the interpretation of Cesarsky et al. (1996b) and Contursi et al. (1998) we would expect a continuum towards 15 μm steeper than that observed in Peak C. Fig. 15 shows that this is not the case. The high 15/6.75 μm value observed is due to the nearly complete absence of AIB carriers and of continuum at short wavelengths (which is instead present in peak C). This dramatically lowers the flux in the LW2 filter. The LW2 and LW3 fluxes of this region are respectively $\simeq 8$ and $\simeq 4$ times smaller than those of peak C in the same filters. The contribution of the [Ne III] emission line in the LW3 filter is only $\simeq 10\%$. We remark that this region is close to the earliest–type star of N66 (OIII(f*)) suggesting that here the ISRF is not only very strong but also very hard. This results in a complete destruction of the AIB carriers and partially also of the smallest VSGs. The VSGs might also be destroyed in the other peaks, although to a lesser degree. This might explain why even if the ISRF throughout the N 66 region is least 10^2 times that of the H II region N 4 in the LMC, the 15/6.75 μm ratios are similar to those found in N 4 (Contursi et al., 1998).

Finally, we show on Fig. 16 a LW10 (8.0–15.0 μm = IRAS 12 μm) filter map superimposed on the DSS image: comparison with Figs. 5 and 10 demonstrates that this image contains features of both maps at 6.75 and 15 μm although it is closer to the 6.75 μm map. While interesting for comparison with IRAS data, the LW10 image is more difficult to interpret than the images in some other filters which have been presented here.

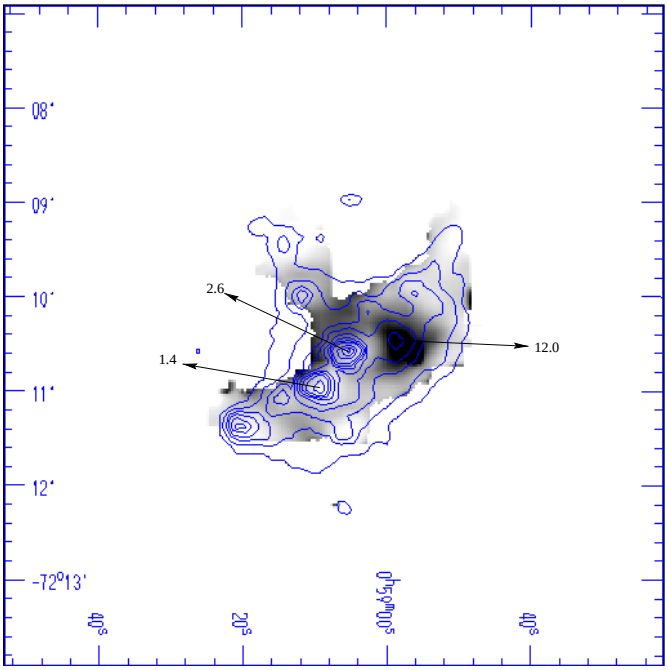

Fig. 13. The LW3(12.0-18.0 μm)/LW2(5.0–8.5 μm) color map (grey scale) superimposed on the LW3 map (contours). Coordinates are J2000. The peak of the map is at the same location of the peak at $\simeq$ 0h 58m 58s -72° 10′ 32″ in Fig. 11. Ratios at some positions are indicated.

6. Discussion and conclusions

We have presented CVF and multi–filter ISO observations of the region of N 66 in the SMC. They reveal a wide variety of phenomena that are not always easy to interpret. The following results have been obtained:

i) Emission in the fine structure line [Ne III] 15.6 μm and [S IV] 10.5 μm is present throughout the region. These line are very strong compared to line from singly–ionized ions like [Ne II], due to excitation by the very hot stars of N 66. There are considerable differences between the space distributions of the [Ne III] and [S IV] line, that we attribute to density effects in the photoionized regions and to shock excitation in a supernova remnant.

ii) AIB emission is generally weak but present in many places of the field. This general weakness, already noted by Sauvage et al. (1990), can be related to the low carbon abundance in the SMC, which is 14–20 times smaller than in our Galaxy (Pagel 1993; Garnett et al. 1995). However, the mid–IR spectrum of a quiescent region in the SMC (Reach et al. 2000) is similar to the galactic "cirrus" emission, suggesting that the differences observed in N66 are principally produced by the extremely high and hard ISRF. Analogous ISOCAM observations of another HII region in the SMC (SMCB1), not yet completely reduced, will help us to clarify which parameters affect the dust properties. There is AIB emission probably coming from the surface of a molecular cloud, like in the region of N 4 in the LMC (Contursi et al. 1998). Most of the AIB spectra we have obtained (see examples in Fig. 6) are different from the classical

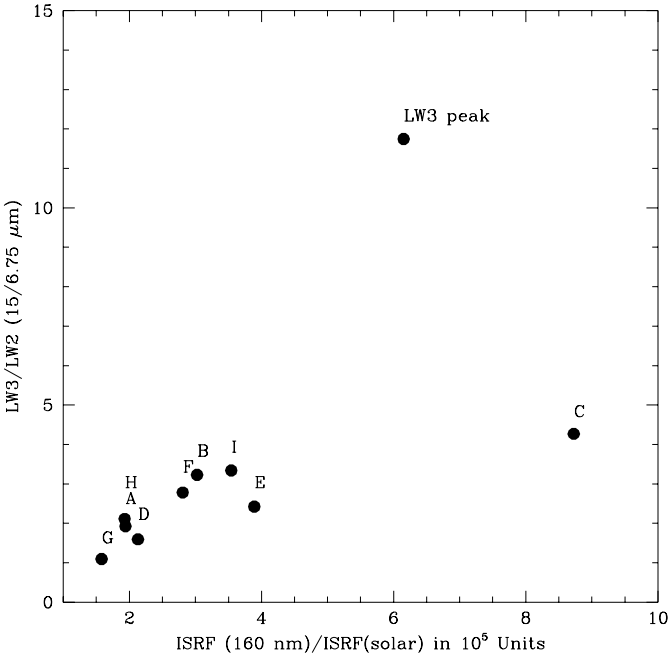

Fig. 14. The LW3(12.0-18.0 μm)/LW2(5.0–8.5 μm) ratios of each peak as a function of the average ISRF at 1600 Å normalized to the local value of the ISRF at the same wavelengths in 10^5 unit. These values have been obtained over the same aperture (2.8 pc of radius) for each peak.

"Galactic" AIB spectra, e.g. those of the reflection nebula NGC 7023 (Cesarsky et al. 1996a). The 7.7 μm feature is almost al-

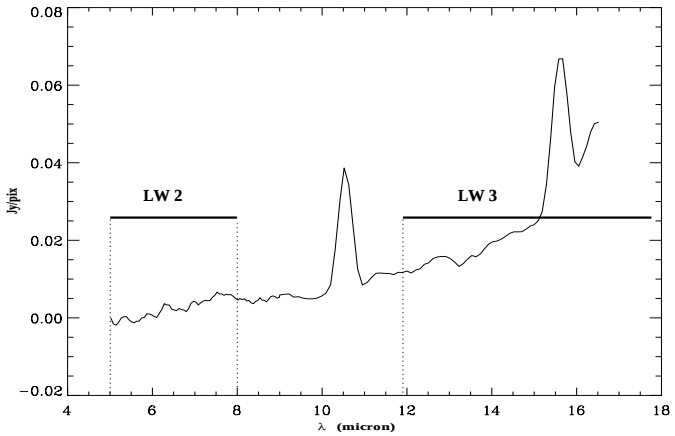

Fig. 15. The CVF spectrum of the region with the largest value of the LW3(12.0-18.0 μm)/LW2(5.0–8.5 μm) ratio.

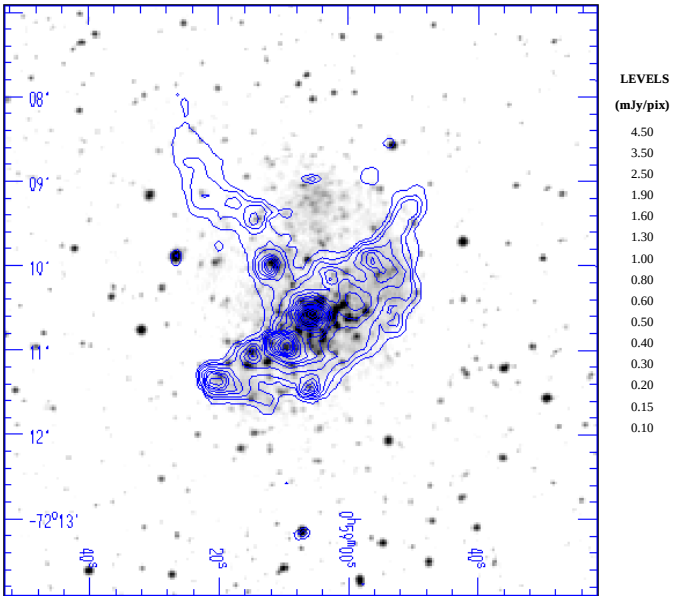

Fig. 16. The LW10 (8.0–15.0 μm = IRAS 12 μm) image superimposed on the DSS image. Coordinates are J2000. Compare to Fig. 5 (LW2 map), Figs. 11 and 12 (LW3 map) and Fig. 13 (LW7 map): there is a mixture of the features of all these maps in the LW10 image, making the latter more difficult to interpret.

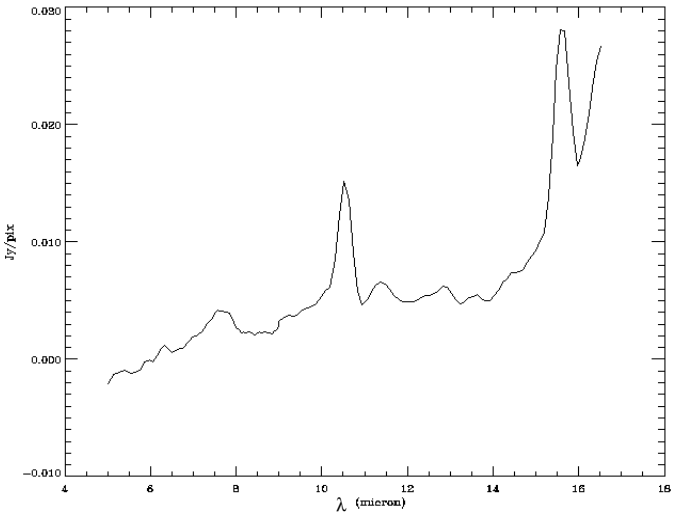

Fig. 17. The average zodiacal–light subtracted CVF spectrum of N66 averaged over the whole CVF ($3' \times 3'$) field, corresponding to a physical size of 53 pc $\times$ 53 pc.

Table 1. The global 15/6.75 μm ratios integrated over the CVF and filter fields of view ($3' \times 3'$ and $7' \times 7'$) of the N66 (SMC) and N4 (LMC) HII regions

HII Region	apparent size	15/6.75 ratio	Physical size (pc)
N66 (SMC)	$3' \times 3'$	3.3	57
N4 (LMC)	$3' \times 3'$	1.6	48
N66 (SMC)	$7.8' \times 7.8'$	1.2	138
N4 (LMC)	$6.4' \times 6.4'$	1.2	96

ways broader than in the ISM of our Galaxy and the 8.6 μm AIB is not always visible (merged with the 7.7 μm feature?). The 11.3 μm band can be strong with respect to the other AIBs, but it can also be quite weak. Also interesting is the fact that the bands at 13.5 and 14.5 μm seem stronger than what is observed in the Galaxy. A similar wide variety of AIB spectra is seen in compact or ultra–compact H II regions (Cesarsky et al. 1996b, Roelfsema et al. 1996).

This variety is presumably due to the co–existence of several forms of AIB carriers, one of which dominates depending on the conditions. The spectrum in the direction of Peak G (close to the edge of the molecular cloud) is not conspicuously different from the classical Galactic AIB spectrum. This cloud is not associated with the N 66 bar. However the 11.3 μm band is somewhat stronger and overall the spectrum is very similar to the spectrum of the molecular cloud M 17N (Henning et al. 1998). The spectrum of peak E is similar to that of very small 3–D carbonaceous grains like semi–anthracite, which also reproduces well the spectra of a few Galactic proto–planetary nebulae (Guillois et al. 1996). None of our spectra matches well that of nanoparticules produced by laser pyrolysis of hydrocarbon (Herlin et al. 1998), at least in the 11-14 μm spectral range. Together with other data, our data will allow the study of the dependence of the AIB spectra on the far–UV radiation density and spectral hardness. Maps of the radiation field like the one presented in Fig. 7 will be useful for such studies.

iii) The ISRF in the bar of N66 is at least 10^5 times the local ISRF at the same wavelength. We have evidence that such strong and hard ISRFs are able to significantly destroy AIB carriers and to a lesser extent also the VSGs.

iv) Aside from the carbonaceous grains just discussed, our observations show continuum emission by silicate grains at several MIR peaks.

Our observations also shed light on the evolution of the N 66 region. Its general optical and mid–IR morphology (Fig. 5) suggests that star formation has arisen in an arc of material compressed by shocks, probably caused by previous supernovae

explosions. There are many examples of similar phenomena in both the SMC and the LMC: HI bubbles (Staveley–Smith et al. 1997, Kim et al. 1998), secondary star formation on the edge of these super bubbles (Parker et al. 1992). This secondary star formation itself is probably not coeval. In fact, peak C contains only unredenned OB stars and it is more evolved than other peaks. Peaks E, H and I for example, have reddened stars suggesting that the surrounding material has not been yet spread out. Following the model proposed by Elmegreen (Elmegreen 1995), we suggest that star formation along the N66 bar has taken place in a sequential way, starting from the OB stars associated to the peak C. The spatial separation between the sub-groups of stars associated to the different MIR peaks is $\simeq$ 8–10 pc, comparable to that predicted by numerical simulations (Elmegreen 1995). Also the nature of dust changes along the bar (Fig. 6) probably because it forms at different times and in different environments. Some of the spectra presented in Fig. 6 show weak S(0)(9.6 μm) and perhaps S(3) (7.0 μm) line of H_2 in emission. This indicates that some molecular gas is still present in the HII region. New CO(2–1) data seem also support this scenario and show that the MIR peaks correspond to molecular clumps with different velocities (Rubio et al. 2000).

Several processes can explain the variety in the observed AIBs strengths and shapes. The AIBs faintness can be ascribed to a significant destruction of their carriers, either by the harsh ISRF or by shocks produced by stellar winds. Broader than normal AIBs can arise from different grains excited by the ISRF of N66; their emission can be generally hidden by the AIBs where these carriers are not significantly destroyed. Other possibilities are that the original grain size distribution is modified by photo–processing on grains, grains shattering, or that the grain composition was originally different due to the low metallicity of SMC. However, this last hypothesis seems to be discarded from the presence of classical Galactic AIBs in a quiscent region of SMC. Finally, the observed variation in the MIR spectra can be related to the the fact that the dust formed at different times and in different environments according to the idea that in N66 the star formation evolved in a sequential way.

The results obtained from the analysis of ISO observations of nearby objects (HII regions, PDRs, molecular clouds, etc.) are useful to understand the dust properties of the more distant galaxies. It is thus important to give the global properties of these nearby regions on scale lengths comparable with the ISOCAM resolution of at least moderately distant galaxies. As LW2 and LW3 are by far the most used filters for ISOCAM observations of external galaxies, we give in Table 1 the 15/6.75 μm (LW3/LW2) ratio of N 66 for two different fields of view: $3' \times 3'$ (CVF field of view) and $7.8' \times 7.8'$ (broad band images), with their corresponding physical sizes. This ratio has been calculated directly on the broad–band images. For comparison we also give in Table 1 the same results for the HII region N 4 in the LMC, for which ISOCAM broad–band data have been already published by Contursi et al. (1998). We also show on Fig. 17 the spectrum of N 66 averaged over the total CVF field of view. Note that N 4 is bathed in a ISRF 100 times lower than the N 66 ISRF. At a scale length of $\sim$ 100 pc there are no significant differences in the mid-IR colors of these HII regions despite their different ISRF. Moreover, on the 100 pc scale, the LW3/LW2 ratios of both N 4 and N 66 are not very different from those found in regions bathed in ISRFs similar to the Local one. The ISOCAM resolution of $\sim 7''$ corresponds to a 100 pc region for an object at a distance of $\sim$ 3 Mpc, that of galaxies in the Sculptor group for example.

Acknowledgements. This research has been supported by the ECOS program of collaboration between France and Chile under grant C97U03. M.R. wishes to acknowledge support from FONDECYT (Chile) grant N.^{0} 1990881

Appendix A: building the 160 nm ISRF map of N 66

We first determined the emission of the stars of N 66 at 160 nm from their magnitudes and spectral types, using the (160 nm - U) colors tabulated in Nandy et al. (1976). We considered all the 88 OB stars catalogued by Massey et al. (1989) except a few for which a spectral type cannot be assessed. 42 of these stars have spectral types given in Massey et al. (1989). For the remaining stars we evaluated the spectral type from their (B-V) and (U-B) colors and from the catalog of Azzopardi & Vigneau (1975). The colors have been corrected for reddening assuming E(B-V)=0.14 for the stars in the N 66 cluster (Massey et al. 1989) and E(B-V)=0.09 for stars catalogued in Azzopardi and Vigneau (1975), the latter value being the mean one for the field stars in the SMC (Garmany et al. 1987). Once a 160 nm flux was assigned to each star, we calculated the radiation density at this wavelength in the region. In order to derive the geometry of the OB association, we had to eliminate the contribution of the diffuse emission from the optical image. We have thus evaluated in the DSS image the emission contribution at five different spatial frequencies. The image corresponding to the smallest spatial frequency ($2''$) represents the stars themselves. We fitted the stellar density distribution by an elliptical gaussian profile for the stars belonging to the OB association. We then assumed that the depth of the cluster is equal to the minor axis of this profile, and assigned to each star a random depth coordinate so that the result fits the chosen radial distribution. For the rest of the stars we did not take into account their depth distribution which anyway is unknown, and assumed that they are all at the same distance. This has little consequence as they are isolated or in small compact groups. We then calculated the 160 nm 3–D radiation density smoothed in cubes whose projection on the plane of the sky correspond to the DSS pixel size ($1.7''$).

Appendix B: stars detected in the N 66 field

A number of stars are visible and identified in the LW2 (5.0–8.0 μm) image displayed Fig. 5. The fluxes we measure are given in Table B.1 together with optical photometry from Massey et al. (1989). For the two red supergiants N 346-283 and 811, the flux ratio LW2/V (6.75/0.55 μm) is about 0.4, compared to the ratio of 0.2 obtained for the red supergiant WOH 53 in the LMC (Contursi et al. 1998). The difference is not very significant and

Table B.1. Stars visible in the LW2 image and in Massey et al. (1989)

Star	Spectrum	V	$U-B$	$B-V$	$6.75\mu m$ (mJy)	Remarks
N 346-283		13.38	2.52 ::	1.68 ::	7.0	Red supergiant
N 346-568		15.97 :	−0.83	−0.14	14.2	
N 346-593	$O5.5V + neb$	14.96	−1.01	−0.16	18.5	in N 66A
N 346-755	$OB? + WN$	11.52 ::	−0.85	−0.24 ::	16.6	HD 5980, var.
N 346-811		14.16	2.68 ::	1.61 ::	3.1	Red supergiant candidate

we cannot say if we observe the photospheric emission of a M supergiant at an approximate effective temperature of 3000 K, or a hotter supergiant with some circumstellar emission. A deeper optical and near–IR study is necessary to solve this ambiguity.

The mid–IR emission of the hotter stars is much too strong to be photospheric, and must be either circumstellar or due to some interstellar material heated by the star. All these emissions are unresolved by our observations. In the case of star N 346-593 which is the brightest of the 7 (or more) exciting stars of N 66A, the mid–IR emission is clearly due to interstellar dust heated by the star. In the other cases the emission might be circumstellar since the stars are apparently isolated and in relatively gas–free regions. The most interesting case (the only one for which we have CVF observations) is that of HD 5980. In this direction, the AIBs at 8.6, 11.3 and 13.5 μm are visible while they are absent in the surrounding area. This indicates carbon–rich dust around the star. It is dubious that this dust is circumstellar, since the star is classified OB?+WN. It is however a very peculiar object which deserves more observations before definitive conclusions can be reached.

References

Abergel A., Bernard J.-P., Boulanger F., et al., 1996, A&A 315, L329
Acosta–Pulido J.A., Klaas U., Laureijs R.J., 1996, A&A 315, L121
Azzopardi M., Vigneau J., 1975, A&AS 22, 285
Biviano A., Sauvage M., Gallais P., et al., 1999, Experimental Astronomy. in press
Boulade O., Sauvage M., Altieri B., et al., 1996, A&A 315, L85
Boulanger F., Reach W.T., Abergel A., et al., 1996, A&A 315, L325
Cesarsky C.J., Abergel A., Agnèse P., et al., 1996, A&A 315, L32
Cesarsky D., Lequeux J., Abergel A., et al., 1996a, A&A 315, L305
Cesarsky D., Lequeux J., Abergel A., et al., 1996b, A&A 315, L309
Cesarsky D., Jones S.P., Lequeux J., et al., 2000, A&A 358, 708
Cohen M., Tielens A.G.G.M., Allamandola L.J., 1985, ApJ 299, L93
Cohen M., Kevin V., 1989, AJ 98, 1563
Contursi A., Lequeux J., Hanus M., et al., 1988, A&A 336, 662
Contursi A., Lequeux J., Cesarsky D., et al., 2000, in preparation
Coulais A., Abergel A., 1999, In: Cox P., Kessler M.F. (eds.) The Universe seen by ISO. ESA SP-427, p. 61
Dale D.A., Helou G., Silbermann N.A., et al., 1999, AJ 118, 2055
Dale D.A., Silbermann N., Helou G., et al., 2000, AJ accepted
Davies R.D., Elliott K.H., Meaburn J., 1976, Mem. R. Astron. Soc. 81, 89
Dennefeld M., Stasińska G., 1983, A&A 118, 234
Désert F.-X., Boulanger F., Puget J.-L., 1990, A&A 237, 215
Dufour R.J., Harlow W.V., 1977, ApJ 216, 706
Dufour R.J., Shields G.A., Talbot R.J. Jr., 1982, ApJ 252, 461
Dwek E., Arendt R.G., Fixsen D.J., et al., 1997, ApJ 475, 565
Elmegreen B.G., Kimura T., Tosa M., 1995, ApJ 451, 675
Garnett D.R., Skillman E.D., Dufour R.J., et al., 1995, ApJ 443, 64
Garmany D.C., Conti P.S., Massey P., 1987, AJ 93, 1070
Gillett F., Forresr W., Merrill K., 1973, ApJ 183, 87
Gondhalekar P., Phillips A., Wilson R., 1980, A&A 85, 272
Guillois O., Nenner I., Papoular R., Reynaud C., 1996, ApJ 464, 810
Helou G., Lu N.Y. Wener M. W., et al., 2000, ApJ Letter in press
Henize K.G., 1956, ApJS 2, 315
Henning Th., Klein R., Launhardt R., Lemke D., Pfau W., 1998, A&A 332, 1035
Herlin N., Bohn I., Reynaud C., et al., 1998, A&A 330, 1127
Heydari-Malayeri M., Hutsemékers D., 1991, A&A 243, 401
Heydari-Malayeri M., Rauw G., Esslinger O., Beuzit J., 1997, A&A 322, 554
Israël F.P., Maloney P.R., 1993, In: Baschek B., et al. (eds.) New Aspects of Magellanic Cloud Research. Springer-Verlag, p. 44
Jourdain de Muizon M., Gabelle T.R., Dhendecourst L.B., Baas F., 1986, ApJ 306, L105
Kim S., Staveley–Smith L., Dopita M.A., et al., 1998, ApJ 503, 674
Klein R., Henning Th., Cesarsky D., 1999, A&A 343, L53
Kunze D., Rigopoulou D., Lutz D., et al., 1996, A&A 315, L101
Kutner M.L., Ulich B.L., 1981, ApJ 250, 341
Laney C.D., Stobie R.S., 1994, MNRAS 266, 441
Le Coarer E., Rosado M., Georgelin Y.P., Viale A., Goldes G., 1993, A&A 280, 365
Lutz D., Feuchtgruber H., Genzel R., et al., 1996, A&A 315, L269
Madden S., 2000, Schaerer D., Delgado-Gonzalez R. (eds.) New Astronomy Reviews. Proceedings for JENAM00: The Interply between Massive Stars and ISM
Massey P., Parker J.W., Garmany C.D., 1989, AJ 98, 1304
Mattila K., Lemke D., Haikala L.K., 1996, A&A 315, L353
Metcalfe L., Steel S.J., Barr P., et al., 1996, A&A 315, L105
Moorwood A.F.M., Lutz D., Oliva E., et al., 1996, A&A 315, L109
Mirabel F., Laurent O., Sanders D.B., et al., 1999, A&A 341, 667
Nandy K., Thompson G.I., Jamar C., Monfils A., Wilson R., 1976, A&A 51, 69
Okumura K., 2000, In: Laureijs R. (ed.) ISO Workshop Proceedings: ISO beyond Point Sources: Study of Exyended Infrared Emission. ESA Pub. Series
Pagel B.E.J., 1993, In: Baschek B., et al., (eds.) New Aspects of Magellanic Cloud Research. Springer-Verlag, p. 330
Pagel B.E.J., Edmunds M.G., Fosbury R.A.E., Webster B.L., 1978, MNRAS 184, 569
Parker J.W., Garmany C.D., Massey P., Walborn N.R., 1992, AJ 103, 120
Peimbert M., Torres–Peimbert S., 1976, ApJ 203, 581
Phillips M.M., Aitken D.K., Roche P.F., 1984, MNRAS 207, 25

Puget J.-L., Lèger A., 1989, ARA&A 27, 161
Reach W.T., Abergel A., Boulanger F., et al., 1996, A&A 315, 381
Reach W.T., Boulanger F., Contursi A., et al., 2000, astro-/ph 0007382
Roche P.F., Aitken D.K., Smith C.H., 1989, MNRAS 236, 485
Roelfsema P.R., Cox P., Tielens A.G.G.M., et al., 1996, A&A 315, L289
Rubio M., Lequeux J., Boulanger F., et al., 1996, A&AS 118, 263
Rubio M., Contursi A., Lequeux J., et al., 2000, A&A accepted
Russell R.W., Soifer B.T., Merril K., 1977a, ApJ 213, 66
Russell R.W., Soifer B.T., Willner S.P., 1977b, ApJ 217, L149
Sauvage M., Thuan T.X., Vigroux L., 1990, A&A 237, 296
Schaerer D., de Koter A., 1997, A&A 322, 598
Starck J.L., Abergel A., Aussel H., 1999, A&AS 134, 135
Stasińska G., 1982, A&AS 48, 299
Stasińska G., 1984, A&A 55, 15
Stasińska G., 1990, A&AS 83, 501
Stasińska G., Leitherer C., 1996, ApJS 107, 661
Staveley–Smith L., Sault R.J., Hatzidimitriou D., Kesteven M.J., McConnelle D., 1997, MNRAS 289, 225
Uchida K., Sellgren K., Werner M., 1998, ApJ 493, L109
Verstraete L., Puget J.-L., Falgarone E., et al., 1996, A&A 315, L337
Vigroux L., Mirabel F., Altiéri B., et al., 1996, A&A 316, L93
Vigroux L., Charmandaris V., Gallais P., et al., 1998, In: Cox P., Kessler M.F. (eds.) The Universe as seen by ISO. ESA, SP-427
Walborn N.R., Blades J.C., 1986, ApJ 304, L17
Ye Taisheng, Turtle A.J., Kennicutt R.C. Jr., 1991, MNRAS 249, 722